Mechanics of Advanced Composite Structures

Journal homepage: https://macs.semnan.ac.ir/

Semnan University

ISSN: 2423-7043

Research Article

2D Bond-Based Peridynamic Simulation of Phase Transformation in 3Y-TZP Dental Ceramics Using ABAQUS

Alireza Moradkhani [a], Mohammad Hoseinpour Gollo [a *], Carla Castiglia Gonzaga [b]

[a] *Department of Mechanical Engineering, Shahid Rajaee Teacher Training University, Tehran, 1678815811, Iran*

[b] *School of Health Sciences, Graduate Program in Dentistry, Universidade Positivo, Curitiba, PR, 81280-330, Brazil*

ARTICLE INFO

Article history:

Received: 2024-10-23

Revised: 2026-01-20

Accepted: 2026-02-25

Keywords:

Dental ceramics;

Bond-Based peridynamics;

Finite element;

Fracture;

Damage.

ABSTRACT

In this research, the fracture behavior of 3 mol% yttria-stabilized tetragonal zirconia polycrystals (3Y-TZP) dental ceramics is investigated. The focus is on the tetragonal (*t*) to monoclinic (*m*) phase transformation using ABAQUS and bond-based peridynamics. We conducted two-dimensional simulations of a single grain undergoing uniform dilational expansion within a homogeneous *m*-phase environment. The effects of transformation time, biaxial stress, and strains on fracture were analyzed. It was found that increasing stress in the surrounding *t*-phase elevated the elastic strain energy associated with the transformation. By varying stress from -1.1 GPa to 400 MPa, elastic strain energy started to decrease from 3.41, 3.32, 3.11, and 2.85 pJ at fracture strain values of S_0= 0.00711, 0.00553, 0.00395, and 0.00237, respectively. These correspond to reductions of 83%, 87%, 90%, and 96%. In addition, damage fractions increased from 0.001, 0.002, 0.003, and 0.004 to 0.005, 0.011, 0.022, and 0.058, respectively. This demonstrates the significant impact of applied stress on the fracture mechanics of 3Y-TZP. Moreover, increasing the elemental parameter S_0 from 0.00237 to 0.00711 in the simulations corresponds to a considerable decrease in defect density, resulting in a substantial increase in the total energy required for material division from 0.25 to 2.2 J/m^2.

1. Introduction

Zirconia (ZrO_2) has excellent properties, making it a popular choice for various applications. However, machining this material presents significant challenges due to its inherent hardness, brittleness, and susceptibility to fracture [1]. Achieving high-precision, damage-free holes necessitates careful consideration of machining parameters, tool selection, and strategies to mitigate thermal and mechanical stresses [2]. Previous research has focused on optimizing techniques such as ultrasonic vibration-assisted machining, laser machining, and abrasive waterjet cutting. These methods aim to enhance material removal rates, reduce surface roughness, and minimize the formation of cracks and residual stresses, ultimately improving the functional performance of ZrO_2 ceramic components [3-5].

ZrO_2 ceramics, particularly 3 mol% yttria-stabilized tetragonal zirconia polycrystals (3Y-TZP), are widely used in dental restorations due

*** Corresponding author.**

E-mail address: *m.hoseinpour@sru.ac.ir*

Cite this article as:

Moradkhani, A., Hoseinpour Gollo, M. and Castiglia Gonzaga, C., 2027. 2D Bond-Based Peridynamic Simulation of Phase Transformation in 3Y-TZP Dental Ceramics Using ABAQUS. *Mechanics of Advanced Composite Structures*, 14(1), pp. 27-39.

https://doi.org/10.22075/MACS.2026.35720.1751

to their excellent biocompatibility, strength, and aesthetic properties [6, 7]. The performance of 3Y-TZP is intrinsically linked to the tetragonal (t) to monoclinic (m) phase transformation ($t \rightarrow m$), a phenomenon that can be influenced by factors such as stress state, temperature, and environmental conditions [8]. While this transformation can provide "*transformation toughening*" by slowing crack propagation [9], it can also lead to degradation and crack formation, particularly in moist environments [10].

Computational modeling is crucial in understanding the complex interplay of factors governing the $t \rightarrow m$ transformation and its impact on fracture. While finite element method (FEM) and extended finite element method (XFEM) offer alternatives to experimental fracture testing by simulating crack propagation and predicting brittle fracture, FEM's mesh dependency and XFEM's reliance on accurate crack tip determination present significant limitations [6, 7]. However, this limits their ability to fully predict the material's response under realistic service conditions. Peridynamics (PD), a non-local continuum theory introduced by Silling [11], offers advantages over traditional finite element methods for simulating crack initiation and propagation. Macek and Silling [12] proposed the implementation of PD in ABAQUS. Huang *et* al. [13] expanded the implementation method of bond-based PD in ABAQUS. Bie *et* al. [14] explored the dual implementation of brittle fracture using the PD method in ABAQUS. Beckmann *et* al. [15] examined the sensitivity of mesh and timestep in fracture analysis due to thermal strains, utilizing PD implemented in ABAQUS. PD models have been developed for various materials, including crystalline and polycrystalline structures. De Meo et al. [16] and Zhang et al. [17] demonstrated PD capture of granular fracture; however, more sophisticated grain boundary representations are needed for improved intergranular failure prediction.

This study aims to enhance the understanding of fracture and damage induced by single-grain phase transformation in 3Y-TZP dental ceramics. To overcome the limitations of traditional finite element methods in simulating fracture, we employ bond-based PD in ABAQUS. By focusing on the interactions between material points during the $t \rightarrow m$ transformation, this research will: 1) investigate the influence of transformation time, biaxial stress, and applied strain on fracture; 2) quantify the relationship between these factors and the resulting elastic strain energy and damage accumulation; and 3) provide insights into the failure mechanisms of 3Y-TZP under phase transformation conditions. This approach, leveraging PD's ability to model crack initiation and propagation without predefined crack paths, will contribute to a more comprehensive understanding of fracture behavior in 3Y-TZP, ultimately aiding in the design of more durable and reliable dental restorations.

2. PD Details

In this study, the dynamic processes of metamorphosis and fracture in 3Y-TZP are modeled by integrating the bond-based PD method into ABAQUS version 2020. This approach builds upon the methodology proposed by Beckmann *et* al. [15] and further refined by Huang *et* al. [13] within the ABAQUS framework. A comprehensive explanation of the implementation of the bond-based PD method in ABAQUS can be found in Huang *et* al. [13]. The following sub-sections will delve into various aspects of the study, including the simulation setup in ABAQUS, a comparison of PD and FE methods, the systematic process for integrating PD simulations within ABAQUS, boundary conditions, and the externally applied loading conditions.

2.1. Simulation Setup in ABAQUS

This approach utilizes the explicit version of PD, which represents the material as a collection of material points linked together through a system of truss components. Each node carries a mass element, and the material's volume is defined by the spacing between these points, calculated based on the material's density. Forces are transmitted between nodes within a specific horizon (h), which is a circular or spherical region surrounding each node. The size of this horizon, determined to be three lattice or material point spaces, was found to provide accurate results while maintaining reasonable computational efficiency.

To ensure the correct bulk material elastic response, the truss elements carrying the force needed to be calibrated. Truss elements, which represent the connections between individual material points (nodes) in the PD model, were calibrated to accurately reflect the material's elastic behavior. To match the elastic modulus of 3Y-TZP, which is 210 GPa [18], the stiffness of the individual truss elements was carefully adjusted through a series of simulations. In the bond-based 2D simulation of PD, akin to a method based on pair potentials at the level of individual atoms, the Poisson's ratio was set at 0.3 [6]. This approach is analogous to how interactions between atoms are modeled in molecular dynamics simulations, where forces depend on the distance between atoms. A mesh comprised of square FE was connected to the PD mesh to determine strain components ε_{11}, ε_{22}, and ε_{12} for

the network of truss elements. Since the continuum elements themselves do not contribute to the stress calculations, they were assigned a negligible elastic modulus, E = 1 Pa, to ensure that the truss elements accurately represented the force transmission.

In the implemented bond-based PD approach, the material mass is concentrated at individual nodes, while the density of the truss elements connecting these nodes is intentionally set to a very low value of 5.5×10^{-10} g/cm^3. This ensures that the total mass of the material is accurately represented by the point masses assigned to the nodes, resulting in a bulk density equivalent to that of 3Y-TZP, specifically 6.1 g/cm^3 [19]. Damage is introduced into the PD model by applying a critical level of mechanical strain to the truss elements in the external region, leading to crack formation when this critical strain is exceeded. The critical fracture strain (S_0) is determined by the strain energy release rate, defined by Silling *et* al. [20], and calculated using equation 1, which quantifies the energy needed to create new surfaces based on the Griffith criterion:

$$S_0 = \sqrt{\frac{5\pi G_0}{9hE}} \tag{1}$$

where h represents the horizon distance, and G_0 denotes the total energy per unit crack surface required for the complete separation of two material halves, as discussed in the work by Kilic and Madenci [21]. The variable S_0 is a key focus of investigation in this context. In this research, simulations were conducted with four values of S_0: 0.00711, 0.00553, 0.00395, and 0.00237. The selected parameters are determined based on stress-strain tailored for 3Y-TZP dental ceramic.

After a truss element reaches the S_0 and fails, its elastic modulus becomes negligible, which is E = 1 Pa. A fracture model based on zero-order kinetics was utilized, indicating that once S_0 is attained, the truss stiffness is reduced without any additional strain [22, 23].

In bond-based PD, damage is typically modeled using a scalar damage variable *d*. *d*, which ranges from 0 (undamaged) to 1 (completely damaged). The bond force between two material points is modified based on the damage state, which can be expressed in equation 2 [24]:

$$f_{ij} = (1-d) f_{ij}^0 \tag{2}$$

where f_{ij} is the actual bond force, f_{ij}^0 is the bond force in the undamaged state, and d is the damage variable. The evolution of the damage variable d is often governed by a damage evolution law, which can be based on stress thresholds or strain energy release rates. A common approach is to define the damage in equation 3:

$$\frac{d}{dt} = \frac{1}{T}(\sigma - \sigma_c) H(\sigma - \sigma_c) \tag{3}$$

where T is a characteristic time scale, σ is the current stress, σ_c is the critical stress threshold, and H is the Heaviside step function. This formulation allows for the gradual introduction of damage as the material experiences loading beyond its elastic limit. However, the lack of detailed explanation regarding the selection of parameters and the specific criteria for damage initiation and propagation may lead to inconsistencies in modeling fracture behavior. The damage equations used in this work are detailed in Huang *et* al. [13].

The study verified PD in the ABAQUS FE framework using a 2D plate under plane strain conditions with a circular cutout under uniaxial tensile stress. Elastic stress concentration slightly exceeded 3, with both PD and FE simulations meshing the hole accurately. PD applied load and boundary conditions, creating two levels within the dental material to eliminate surface effects, achieved by transforming a FE grid into a phase-field mesh and introducing a hole. The implementation details for PD and FE, including dimensions, properties, and simulation parameters for the 3Y-TZP simulation, are outlined in Table 1.

Table 1. PD and FE details for 3Y-TZP simulation

Parameter	PD	FE
3Y-TZP width	1 m	1 m
Density of 3Y-TZP	6.1 g/cm^3 [19]	6.1 g/cm^3 [19]
External applied load	2×10^4 Pa	2×10^4 Pa
Central grain radius	6×10^{-7} m	6×10^{-7} m
Horizon radius	3×10^{-7} m	3×10^{-7} m
Material point spacing	1×10^{-7} m	1×10^{-7} m
Pressure (atm)	1	1
Poisson's ratio	0.3	0.3
Elastic modulus	210 GPa [18]	210 GPa [18]
Temperature (°C)	27 °C	27 °C
Number of elements	3480	2880

Figure 1 illustrates a flowchart outlining the step-by-step process for implementing PD simulations using ABAQUS, as applied in this study. The investigation omits the impact of anisotropy in dental ceramics to enhance and streamline the analysis. Simulations were conducted with four different S_0 values to ensure the accuracy of the average values.

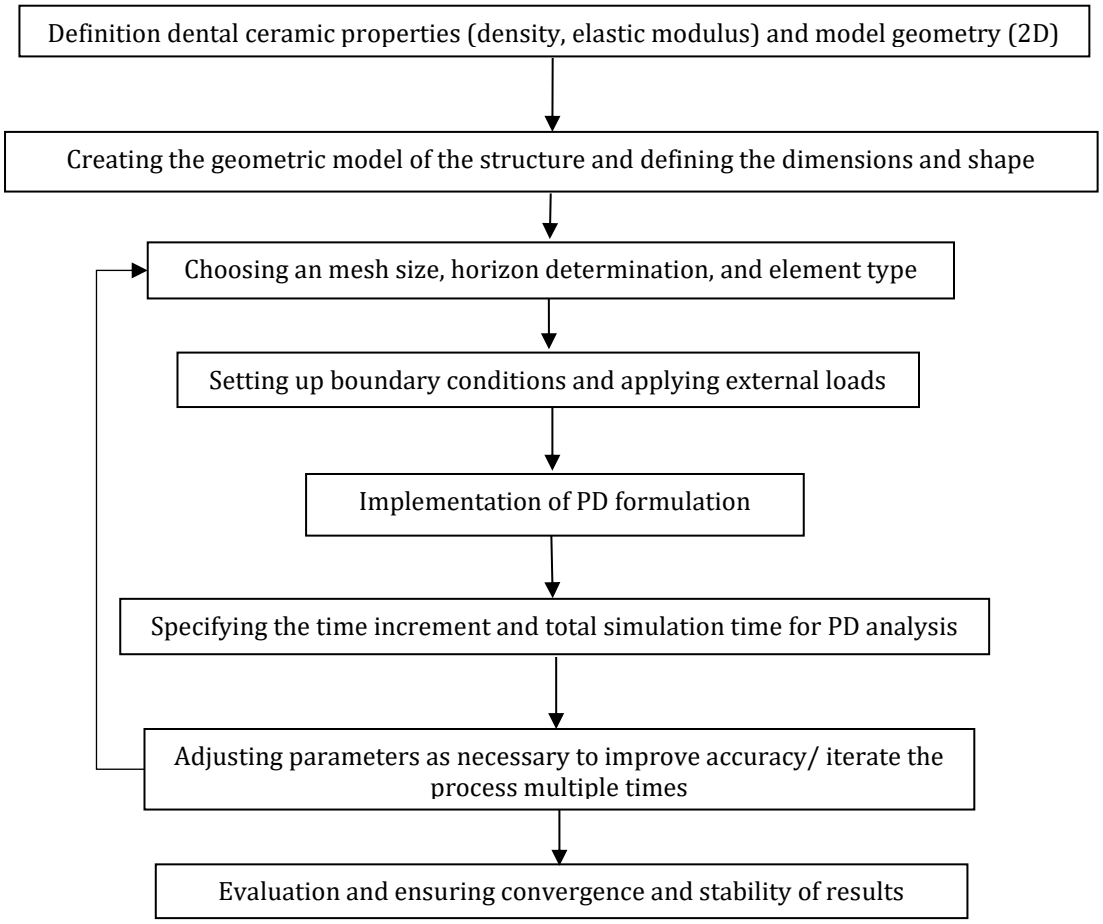

Fig. 1. Flowchart outlining the systematic procedure for implementing peridynamics simulations within the ABAQUS framework

Symmetry boundary conditions were applied to mitigate artificial edge effects in 3Y-TZP, restricting displacement perpendicular to certain edges while allowing displacement parallel to them. Used ABAQUS FE simulation for nodal displacement calculation, which was applied to specific nodes to induce compressive and tensile stress conditions.

This method ensures a uniform stress distribution across the model. The phase transformation was simplified as a dilatational volumetric expansion, modeled by magnifying a central group of truss elements based on hydrostatic strain calculations. Deformations were imposed only on the truss mesh, not the continuum mesh, which is linked to the truss mesh for strain mapping purposes.

These detailed simulation and modeling approaches provide a comprehensive framework for studying 3Y-TZP dental ceramics fracture under transformation-induced conditions, offering insights into crack formation and propagation in dental materials.

The simulation setup, as depicted in Figure 2, features a single 3Y-TZP grain surrounded by a homogeneous layer. The model incorporates a combination of continuum elements with reduced integration positioned beneath a lattice of truss elements, representing the PD mesh. The simulation covers a 25×10^{-12} m^2 surface area, with a central grain radius of 6×10^{-7} m. As detailed in Table 1, the material point spacing is 1×10^{-7} m, establishing a horizon radius of 3×10^{-7} m. Initial parametric investigations determined the maximum feasible model size relative to the central grain, considering available computational resources. Unlike traditional methods that rely on strain, PD formulation uses a different approach. It represents the 3D model with a finite thickness determined by the size of the material points.

In Figure 3, the central grain volume is depicted for both PD and FE simulations, under conditions identical to those in Figure 2. Table 1 indicates that a unit grain width of 1m is being considered.

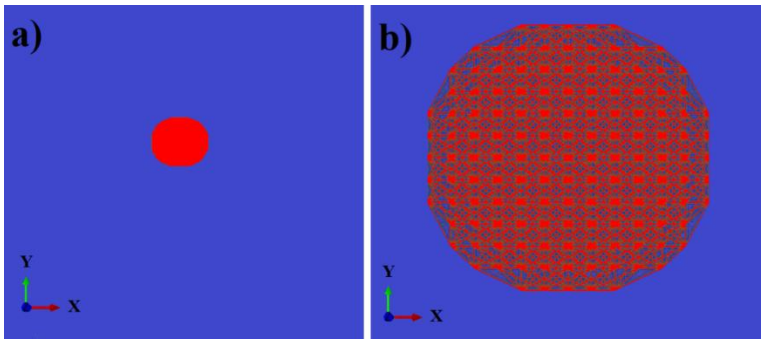

Fig. 2. a) Full model; b) truss element mesh

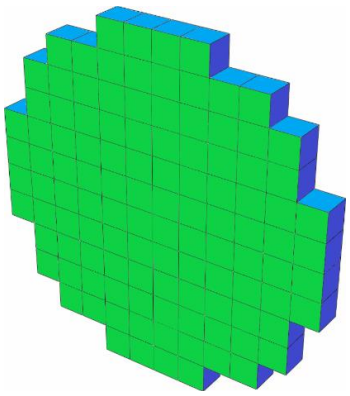

Fig. 3. Central grain volume in PD and FE simulations for 3Y-TZP

2.2. Boundary Conditions and Stress Application

Figure 4 illustrates the application of symmetry boundary conditions to the initial four-node rows at the bottom and left boundaries of the simulation. The determined displacements were subsequently utilized to shift four rows of nodes positioned along the remaining edges of the simulation, causing the nodes to move in a direction perpendicular to the edge faces. To create a uniform stress state throughout the simulation, one edge is immobilized while the opposite edge is subjected to displacement. This method induces a consistent stress distribution across the model.

Subsequently, symmetry boundary conditions are implemented to restrict movement perpendicular to each edge after applying the nodal displacements. These conditions restrict the displacement of the vertical edges while allowing displacement of the parallel edges.

The arrangement of these boundary conditions is detailed in Figure 4, depicting a single transforming grain within a denser dental ceramic.

Additional quantitative characteristics are under the same conditions as detailed in Table 1 and Figures 2 and 3.

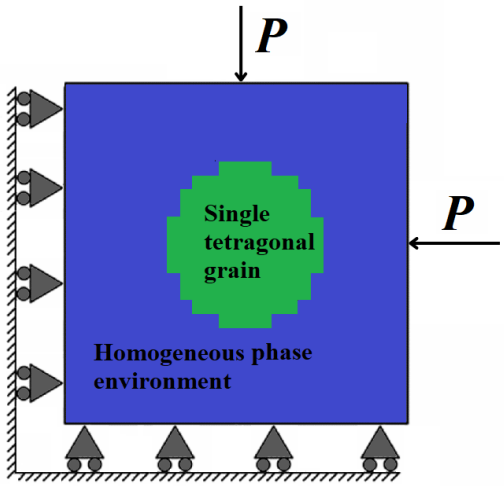

Fig. 4. Imposing boundary conditions and loads (*P*) on a single grain within a homogeneous phase environment

2.3. Tetragonal-to-Monoclinic Transition

In a prior examination utilizing FE analysis, a variety of transformation possibilities were explored, resulting in an expansion in volume of around 6% and a shear strain of approximately 16%, aligning with figures documented in existing literature sources [25-29]. While the specific effects of anisotropic material properties and variant selection are not the primary focus here, to streamline the analysis, the phase transformation is simplified as an increase in volume.

The method utilizes the strain, computed using the strain tensors outlined in the study by Platt *et* al. [30] for oxidation of ZrO_2 alloys and expressed in Eq. 4. $t \rightarrow m$ transformation is simulated as a dilatational growth/volumetric expansion by amplifying a central group of truss elements, as illustrated in Figure 2. The central truss members elongate by 0.02 due to the hydrostatic strain and the strain tensors derived [30]. It is important to note that expansion strains are specifically applied to the truss mesh and not to the continuum mesh. Expansion strains apply only to the truss mesh, according to Eq. 4:

$$\varepsilon_{(100)t/(100)m} = \begin{bmatrix} 0.0013 & 0 & 0.08125 \\ 0 & 0.2647 & 0 \\ 0.08125 & 0 & 0.02924 \end{bmatrix} = \begin{bmatrix} 0.02 & 0 & 0 \\ 0 & 0.02 & 0 \\ 0 & 0 & 0 \end{bmatrix} \quad (4)$$

The maximum rate is constrained by the sonic velocity in 3Y-TZP, a relationship detailed in equation 5 [31]:

$$c_z = \sqrt{\frac{G_z}{\rho_z}} = \sqrt{\frac{83000}{5.68\times10^{-9}}} \quad (5)$$

where c_z represents the sonic velocity in 3Y-TZP, G_z stands for the shear modulus for 3Y-TZP, and ρ_z denotes the density of 3Y-TZP. These values were obtained for polycrystalline material, assuming comparability to single-crystal 3Y-TZP ceramic.

The sonic velocity in bulk 3Y-TZP is calculated to be approximately 3.96×10^6 mm/s, as reported in the work of Moradkhani *et* al. [32]. Assuming grain transformation initiates from the center and spreads outward, the maximum time required for complete transformation of the grain is estimated by dividing the grain radius ($\sim 0.5 \times 10^{-3}$ mm) by the sonic velocity in 3Y-TZP, resulting in a total transformation duration of 1.5×10^{-10} s. While defining the phase transformation rate as equivalent to the sonic velocity poses experimental challenges, some researchers suggest that this transformation may be approximately 1/3 of the sonic velocity [33, 34].

To incorporate this feature into the PD simulation, a progressive increase in truss element length was implemented, reaching a maximum value during the transformation period, simulating the isotropic expansion of the *t* grain. This expansion was uniformly applied to all truss elements in the central area.

The simulation explored various transformation time durations ranging from 5×10^{-11} s to 3.4×10^{-9} s in the parametric study, with a total simulation runtime of 2×10^{-8} s to capture any subsequent damage post-phase transformation. A stable time increment of 1×10^{-12} s was determined using the von Neumann stability criterion.

As a tetragonal 3Y-TZP grain transitions into the *m*-phase, a shift occurs in the energy content related to the grain. This alteration can be precisely defined by the equation 6:

$$\Delta W = \Delta U_{Strain} + \Delta G_C + \Delta U_{Surface} \quad (6)$$

where ΔW signifies the alteration in overall free energy, ΔU_{Strain} denotes the adjustment in elastic strain energy, ΔG_C indicates the alteration in chemical energy balance as the transformation evolves from a less stable parent phase to a more stable product phase, and $\Delta U_{Surface}$ represents the variation in surface energy encompassing boundaries between phases and surfaces of cracks. U_{Strain} and U_{Surface} are positive when chemical energy is negative. The transformation proceeds only if the total free energy change is negative, consistent with previous research [22, 30].

3. Results and Discussion

3.1. Elastic Strain Energy of Transformation

Strain mappings were imposed on the truss mesh in the simulation, using data from the continuum element mesh. Figure 5 illustrates the state of strain (ε_{11}, ε_{22}) on the interconnected mesh enveloping the single grain transforming its core in 3Y-TZP ceramic, without external stress applied, and no fractures observed in neighboring truss elements.

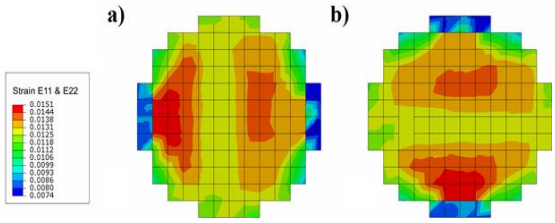

Fig. 5. Components identified by the FE mesh in 3Y-TZP ceramic without stress (a) ε_{11} , (b) ε_{22}

Analyzing the interaction between the solid material and the truss model, specifically within the transforming grain, allows for a precise determination of the change in *U* due to the phase transformation. The strain components for each continuum element were computed by subtracting the recorded strain post-transformation from the strain that would have occurred under unconstrained expansion. Subsequently, the *U* of an individual element can be calculated based on these considerations, particularly within a plane strain formulation, according to equation 7:

$$U_{SU} = A\left((\varepsilon_{11}{}^2 + \varepsilon_{22}{}^2)\frac{vG}{1-2v} + (\varepsilon_{11}{}^2 + \varepsilon_{22}{}^2)G + 2G(\varepsilon_{12}{}^2) \right) \quad (7)$$

The strain components ε_{11}, ε_{22}, and ε_{12} represent the strain components, where G is the shear modulus and A denotes the area of the single grain after $t \rightarrow m$ transformation. This approach is akin to the Eshelby [35], often employed for calculating the elastic field related to an ellipsoid inclusion.

Figure 6 presents a comparison of elastic strain energy. The comparison is between values obtained from a conventional ABAQUS FE simulation (computed using FE strains) and those derived from strains in the PD model. Each data point in the plot corresponds to an individual simulation without fractures.

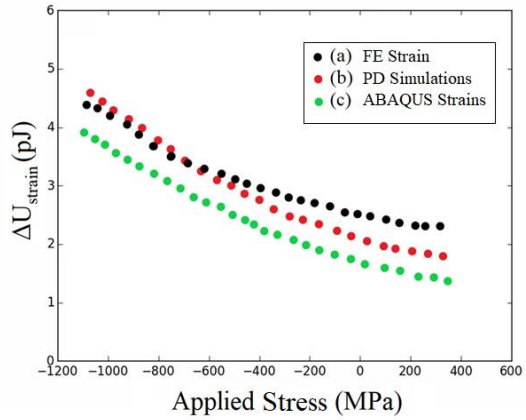

Fig. 6. Energies related to the strain transformation in the grain under applied stress from ABAQUS, Black points (a): FE strain results, Red points, (b): strains in PD simulations results, Green points (c): ABAQUS strain results

The strains in the PD simulations are defined using a continuum mesh with negligible mass and stiffness, anchored to the load-bearing truss element PD network.

The calculated FE of strain energy closely aligns with those from ABAQUS, validating the application of the equation. Strain energy from PD simulations exhibits a similar trend to FE simulations, albeit with an overall reduction of about 13% attributed to the truss elements of lower density expanding along the interface.

Figure 7 overlays the central truss elements to the continuum elements, showing a discrepancy in the number of truss elements expanding at the edge compared to the center.

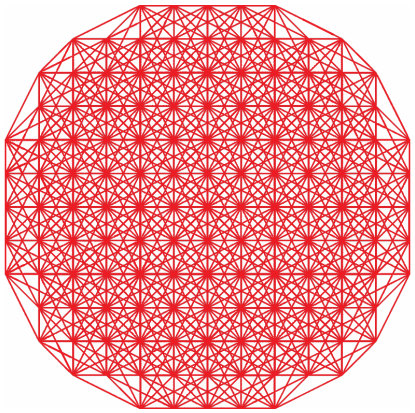

Fig. 7. Overlay of central truss elements on central continuum elements

Figure 8 illustrates the variation for various transformation times in the U of the transformed grain, using S_0 = 0.00237 and without any applied stress. Each data point represents a distinct simulation, showing a significant drop in transformation U below a threshold of approximately 0.4 × 10^{-9} s.

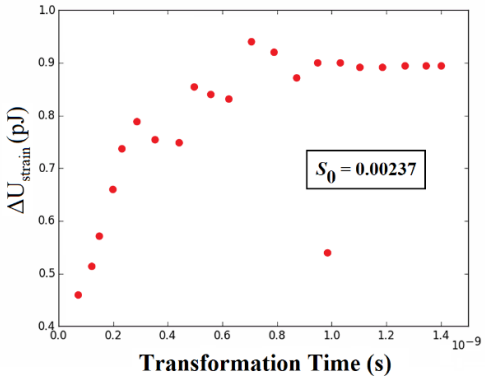

Fig. 8. Influence of transformation time on elastic strain energy change

Figure 9 illustrates simulations for transformation in 2 × 10^{-10} and 2 × 10^{-9} s, highlighting the fractured truss elements and the load bearing in red and blue, respectively. A decrease in transformation time results in more truss elements becoming fractured. Further exploration of the S_0 under varied applied stresses for a transformation time of 2 × 10^{-10} s yielded inconsistent results, leading to the adoption of 2 × 10^{-9} s for the following simulations.

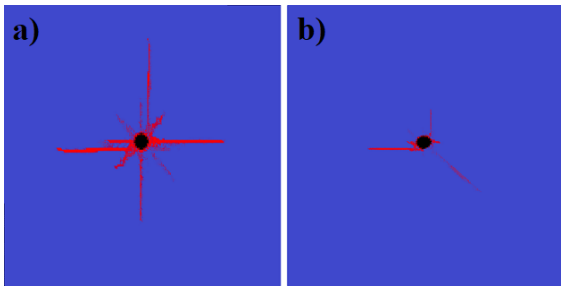

Fig. 9. Fracture profiles at varying transformation times and S_0 = 0.00237, without applied stress, a) 2 × 10^{-10} s and b) 2 × 10^{-9} s

Figure 10 displays elastic strain energy (ΔU_{Strain}) for different applied biaxial stress levels during a 2 × 10^{-9} s transformation in various S_0 states. The data includes the S_0 for simulations without fractures, denoted as "No Fx." The link between the S_0 and applied stress closely follows a linear trend when fracture is disallowed, particularly under predominantly compressive stress. The impact of S_0 becomes increasingly notable as the applied stress shifts towards tensile stress, deviating from linearity at lower compressive stress levels. As depicted in Figure 10, by adjusting the stress values within the range of -1.1 GPa to 400 MPa over a time span of 2 × 10^{-9} s, and considering fracture strain values of S_0= 0.00711, 0.00553, 0.00395, and 0.00237, the corresponding elastic strain energy decreased from 3.41, 3.32, 3.11, and 2.85 pJ to 0.61, 0.44, 0.32, and 0.1 pJ, respectively.

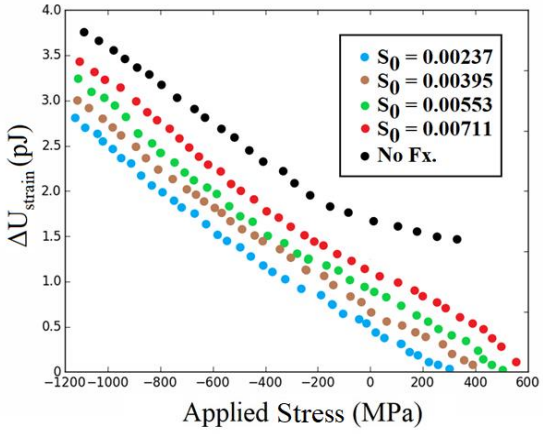

Fig. 10. Exploring elastic strain energy fluctuations under diverse bi-axial stress scenarios in 2 × 10^{-9} s

Figure 11 presents this study's average elastic strain energy results (black line), compared with experimental data from the literature for 3Y-TZP. For this purpose, elastic strain energy density is calculated by equation 8 [23]:

$$U = \frac{1}{2}\sigma\varepsilon V \tag{8}$$

where σ is stress, ε is strain, and V is volume. For linear elastic materials, this can also be expressed by equation 9:

$$U = \frac{1}{2}\frac{\sigma^2}{E}V \tag{9}$$

where E is the elastic modulus, leading to strain energy per unit volume as expressed by equation 10:

$$u = \frac{1}{2}\frac{\sigma^2}{E} \tag{10}$$

Figure 11 compares the average strain energy ranges calculated via ABAQUS in this study (black line) with ranges derived from the experimental data of previous studies (using Eqs. 8-10). Specifically, applying Eq. 10 to the results of Diaz *et* al. [36] (E = 199 ± 4 GPa, σ = 1071 ± 99 MPa) yielded a strain energy range of 2.37-3.44 pJ (red points). Similarly, calculations based on Vladislavova *et* al. [37] (E = 200 ± 3 GPa, σ = 1000 ± 6 MPa) yielded 1.46-2.16 pJ (blue points), and calculations based on Moradkhani *et* al. [6, 32] (E = 215 ± 7 GPa, σ = 312 ± 7 MPa) yielded 0.88-1.13 pJ (green points). The results of the current study deviate significantly from predictions assuming linear elasticity.

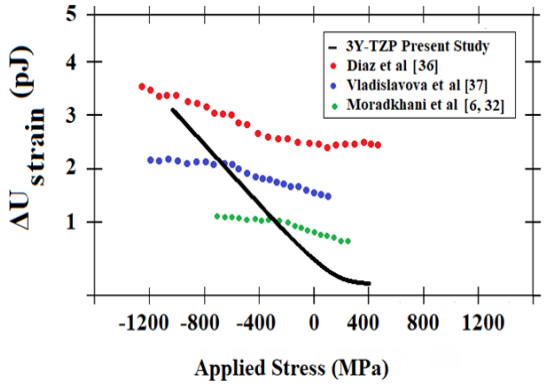

Fig. 11. Average elastic strain energy results of this study, juxtaposed with theoretical data from the literature for 3Y-TZP

3.2. Damage

In the PD simulations, the damage fraction was determined by calculating the proportion of fractured truss elements surrounding the central grain, providing an overall measure of damage for each simulation. In Figure 12, the relationship between damage fraction and applied stress is shown for a transformation time of 2 × 10^{-9} s, revealing a more pronounced impact from bi-axial tensile stress compared to bi-axial compressive stress, similar to the S_0 trends. The relationship between S_0 and the level of damage in the layer surrounding the central grain is evident from a comparison of Figs 10 and 12. Increased fracture reduces the constraint on the transformed grain, resulting in a decrease in U, which is consistent with the findings of Platt *et* al. [22]. As can be seen in Figure 12, by adjusting the stress values within the range of -1.1 GPa to 400 MPa over a time span of 2 × 10^{-9} s, and

considering fracture strain values of S_0= 0.00711, 0.00553, 0.00395, and 0.00237, the corresponding damage fraction increased from 0.001, 0.002, 0.003 and 0.004 to 0.005, 0.011, 0.022, and 0.058, respectively.

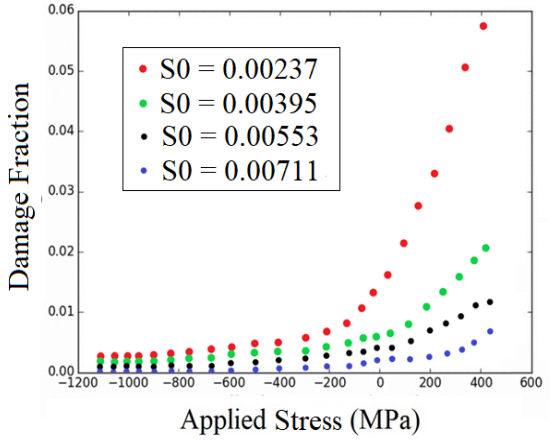

Fig. 12. Relationship between damage fraction and applied stress in truss elements in 2 × 10^{-9} s

Figure 13 shows the maximum principal strain in the transformed grain and fractured truss elements in the homogeneous monoclinic matrix area. This highlights a correlation between regions of high strain in the central grain and areas of significant damage in the external layer. A comparison of Figures 4 and 13 reveals that the principal strain within the tetragonal deformed grain propagates into the surrounding homogeneous monoclinic matrix and damages it. The connection between the damage fraction and the S_0 is not absolute, as illustrated by simulations with similar S_0s but differing damage fractions. This discrepancy suggests that beyond a specific point, further fracture causes minimal impact to the transforming grain.

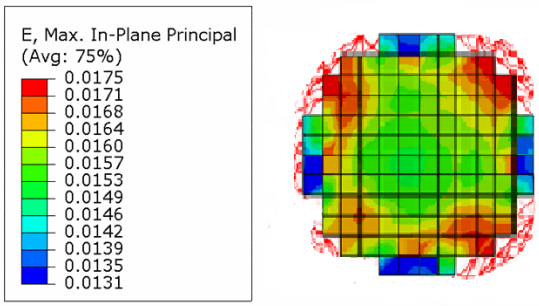

Fig. 13. Maximum principal strain of a central grain onto fractured truss elements near the homogeneous area

Figure 14 presents a range of patterns of fractures for various applied stresses and S_0s, offering a depiction of the damage observed in Figure 12 and insights into the damage mechanisms. Notably, at a stress level of -1.1 GPa, damage manifests as failed truss elements rather than distinct cracks, exerting a substantial influence on the transformation U despite a low damage fraction. The application of tensile stress in two directions aims to replicate the area in front of a crack tip in 3Y-TZP dental applications. Here, crack formation near the external region interface is linked to a reduction in external layer protection. Phase transformation-induced fracture, often linked to nano-pore formation along grain boundaries, can weaken the fracture strength near a transforming grain. While the $t \rightarrow m$ phase transformation in 3Y-TZP can impede crack propagation [19, 32], it also contributes to issues like crack micro-branching and hydro-thermal degradation.

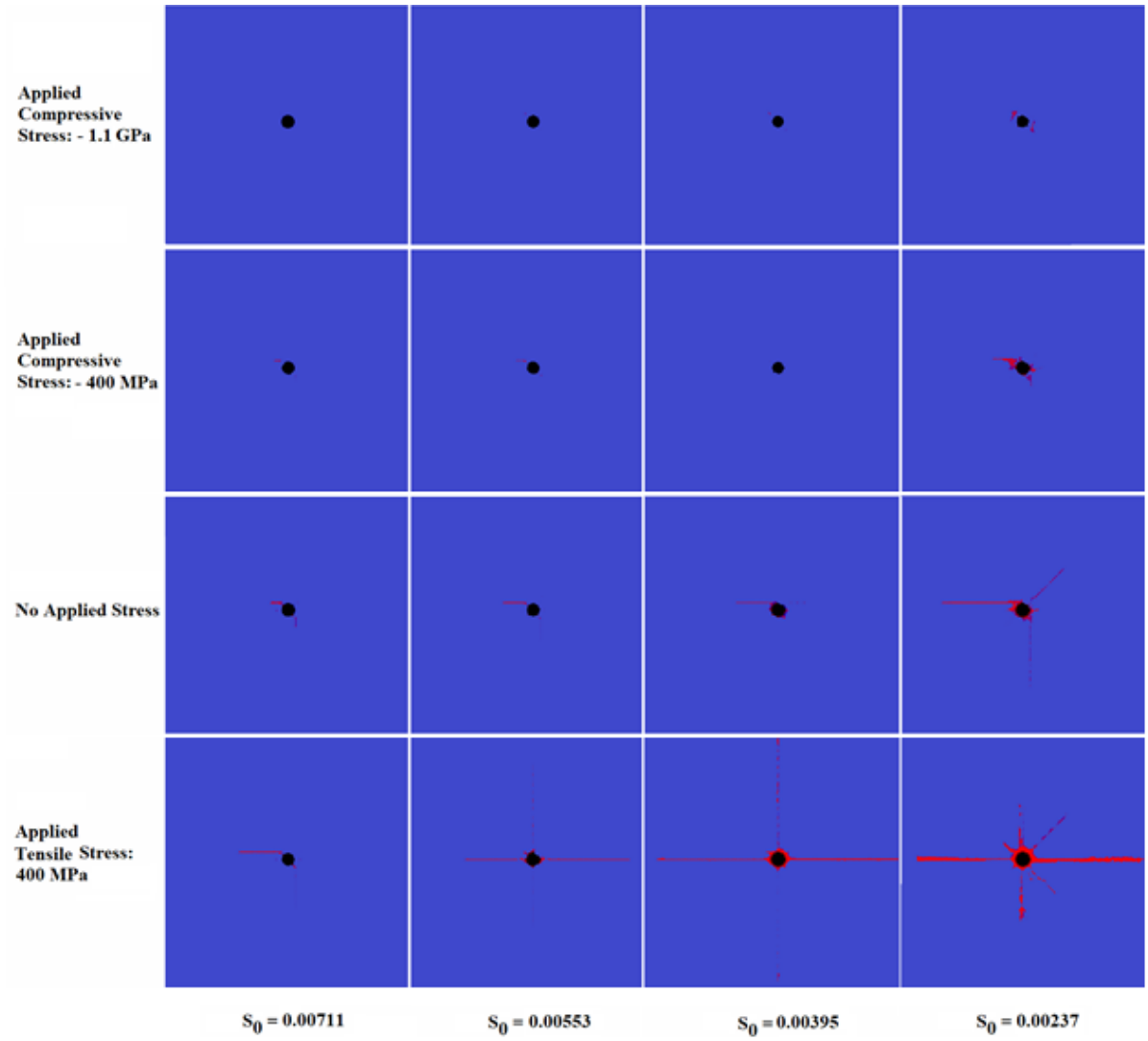

Fig. 14. Analyzing fracture behavior in 3Y-TZP across different applied stresses and S_0s

3.3. Elemental and Superficial Energies

In the context of the simulations, S_0 values of 0.00711, 0.00553, 0.00395, and 0.00237 can be used in Eq. 1 to calculate G_0, representing the total energy needed to divide a material into two parts. These S_0s correspond to G_0 values of 0.25, 0.68, 1.32, and 2.2 J/m² according to Eq. 1. Notably, G_0 primarily reflects the difference in energy density between crack faces and the energy levels of current interfaces and surfaces, including defects and grain boundaries, rather than serving as a direct surface energy density measure. Crack and imperfection density and dimensions impact the fracture resistance of a material.

In the PD simulation context, adjustments to incorporate increased defect density involve reducing S_0 and concurrently G_0. Studies have highlighted non-negligible interfacial energies for monoclinic 3Y-TZP, with coherent and partial interfacial energy densities reported. The literature presents varying numerical values representing the density of free surface energy of monoclinic/tetragonal 3Y-TZP, reflecting the complexity of these properties [22, 38].

Simulations with higher S_0 and corresponding G_0 values indicate microstructures characterized by minimal defects and grain boundaries in the surrounding region, aligning more closely with observations from certain experimental studies [22]. Equations have been proposed to describe Δ_{GC} concerning temperature, indicating that transformation processes may occur independently of applied loads or fracture behaviors under certain conditions [39].

The introduction of oxygen vacancies, through doping such as Al_2O_3 or oxidation processes, can significantly alter Δ_{GC}, potentially influencing phase transformation outcomes. These findings underscore the significance of factors affecting chemical free energy changes in determining phase transformation behaviors in 3Y-TZP dental ceramics.

4. Future Perspectives

This study utilized a bond-based PD approach within ABAQUS to simulate the tetragonal-to-monoclinic phase transformation and its influence on fracture in 3Y-TZP dental ceramics. While this 2D simulation provided valuable insights into the effects of stress and transformation time, it inherently simplifies the complex behavior of the material. Specifically, the 2D limitation neglects out-of-plane expansion, assumes isotropy, and omits shear components, potentially affecting the accuracy and applicability of the results to real-world scenarios.

Future research should prioritize addressing these limitations through the implementation of three-dimensional PD simulations. Incorporating shear components in these 3D models will allow for a more comprehensive understanding of the phase transformation process and its impact on fracture initiation and propagation. Furthermore, given the observed reduced incidence of phase transformation-induced fractures in 3Y-TZP compared to ZrO_2 ceramics, future investigations should directly examine the roles of compressive stress and varying phase fractions in mitigating fracture. These studies could explore the interplay between applied stress, transformation-induced elastic strain energy, and damage accumulation, building upon the relationships identified in this work.

Finally, the influence of common additives such as Al_2O_3, CaO, MgO, CeO_2, and Er_2O_3 on the fracture behavior of 3Y-TZP warrants further investigation. These additives can significantly alter the material's microstructure and introduce anisotropy, requiring advanced modeling techniques to accurately capture their effects. Future studies should focus on characterizing the anisotropic properties of these modified 3Y-TZP ceramics and incorporating these properties into PD simulations to predict their performance under complex loading conditions. This will ultimately contribute to the development of more durable and reliable dental ceramic materials.

5. Conclusions

This study investigated the fracture behavior of 3 mol% yttria-stabilized tetragonal zirconia polycrystals (3Y-TZP) dental ceramics, focusing on the tetragonal (*t*) to monoclinic (*m*) phase transformation using ABAQUS and bond-based peridynamics. Two-dimensional simulations were conducted to analyze the effects of transformation time, biaxial stress, and strains on fracture within a single grain undergoing uniform dilational expansion. The following conclusions can be drawn from this study:

- Increasing stress in the surrounding *t*-phase significantly elevates the elastic strain energy associated with the transformation. Specifically, by varying stress from -1.1 GPa to 400 MPa, the elastic strain energy at fracture decreased from 3.41 pJ to 2.85 pJ at fracture strain values of S_0= 0.00711 and 0.00237, respectively, representing a 16% reduction in elastic strain energy.
- Applied stress has a substantial impact on damage accumulation during phase transformation. Damage fractions increased from 0.001 and 0.004 at -1.1 GPa, respectively, to 0.005 and 0.058 at 400 MPa, demonstrating a significant increase in damage accumulation due to applied stress.
- The simulations demonstrate a direct correlation between the elemental parameter S_0 (0.00237 to 0.00711) and the total energy G_0 (0.25 to 2.2 J/m^2) needed for material division, reflecting the impact of defect density on fracture resistance. Lower S_0/G_0 values indicate higher defect densities, while higher values suggest fewer defects. Ultimately, these parameters influence phase transformation behaviors in 3Y-TZP dental ceramics.
- The 2D simulations suggest that the application of compressive stress and control of phase fraction are important factors in mitigating phase transformation-induced fracture in 3Y-TZP. This implies that optimizing these parameters could lead to the development of more robust dental ceramic materials.

Funding Statement

This research did not receive any specific grant from funding agencies in the public, commercial, or not-for-profit sectors.

Conflicts of Interest

The author declares that there is no conflict of interest regarding the publication of this article.

References

[1] Ji, M., Xu, J., Yu, D., Chen, M. and El Mansori, M., 2021. Influence of sintering temperatures on material properties and corresponding milling machinability of zirconia ceramics. *Journal of Manufacturing Processes*, *68*, pp. 646-656.

[2] Ji, M., Xu, J., Li, L., Yu, D., Chen, M. and El Mansori, M., 2021. Nano-scale mechanical behaviors and material removal mechanisms of zirconia ceramics sintered at

various temperatures. *Ceramics International*, *47*(23), pp. 32588-32598.

[3] Yin, Y., Xu, J., Ji, M., Li, L. and Chen, M., 2023. A critical review on sintering and mechanical processing of 3Y-TZP ceramics. *Ceramics International*, *49*(2), pp. 1549-1571.

[4] Li, L., Xu, J., Ji, M., Yin, Y. and Chen, M., 2022. On crack suppression mechanisms of ultrasonic elliptical vibration cutting of 3Y-TZP ceramics. *Ceramics International*, *48*(19), pp. 28308-28326.

[5] Ji, M., Xu, J., Li, L., Yu, D., Chen, M., Geier, N. and El Mansori, M., 2022. Investigation of material removal mechanisms and ductile-brittle transition zone of zirconia ceramics sintered at various temperatures. *Journal of the mechanical behavior of biomedical materials*, *125*, p. 104944.

[6] Moradkhani, A., Hoseinpour Gollo, M. and Panahizadeh, V., 2025. Effect of Microstructural Features and Al_2O_3 Doping on Aging Resistance, Mechanical Properties and Crack Propagation in 3Y-TZP Plate Ceramics for Dental Restorations: A Comprehensive Peridynamics Study. *Mechanics of Advanced Composite Structures*, *12*(3), pp. 523-554.

[7] Moradkhani, A., Hoseinpour Gollo, M., 2026. Computational fracture analysis of 3Y-TZP dental ceramics with low Al_2O_3 using peridynamics. *Sigma Journal of Engineering and Natural Sciences*, Article in Press. DOI: 10.14744/sigma.2025.1922

[8] Yin, Y., Xu, J. and Chen, M., 2024. A review on surface texturing of zirconia ceramics for dental applications. *The International Journal of Advanced Manufacturing Technology*, *130*(11), pp. 5109-5135.

[9] Andreasen, J.H. and Karihaloo, B.L., 1996. *Mechanics of transformation toughening and related topics* (Vol. 40). Elsevier.

[10] Eichler, J., Rödel, J., Eisele, U. and Hoffman, M., 2007. Effect of grain size on mechanical properties of submicrometer 3Y-TZP: fracture strength and hydrothermal degradation. *Journal of the American Ceramic Society*, *90*(9), pp. 2830-2836.

[11] Silling, S.A., 2000. Reformulation of elasticity theory for discontinuities and long-range forces. *Journal of the Mechanics and Physics of Solids*, *48*(1), pp. 175-209.

[12] Macek, R.W. and Silling, S.A., 2007. Peridynamics via finite element analysis. *Finite elements in analysis and design*, *43*(15), pp. 1169-1178.

[13] Huang, X., Bie, Z., Wang, L., Jin, Y., Liu, X., Su, G. and He, X., 2019. Finite element method of bond-based peridynamics and its ABAQUS implementation. *Engineering Fracture Mechanics*, *206*, pp. 408-426.

[14] Bie, Y.H., Liu, Z.M., Yang, H. and Cui, X.Y., 2020. Abaqus implementation of dual peridynamics for brittle fracture. *Computer methods in applied mechanics and engineering*, *372*, p. 113398.

[15] Beckmann, R., Mella, R. and Wenman, M.R., 2013. Mesh and timestep sensitivity of fracture from thermal strains using peridynamics implemented in Abaqus. *Computer methods in applied mechanics and engineering*, *263*, pp. 71-80.

[16] De Meo, D., Zhu, N. and Oterkus, E., 2016. Peridynamic modeling of granular fracture in polycrystalline materials. *Journal of Engineering Materials and Technology*, *138*(4), p. 041008.

[17] Zhang, T., Gu, T., Jiang, J., Zhang, J. and Zhou, X., 2024. An ordinary state-based peridynamic model for granular fracture in polycrystalline materials with arbitrary orientations in cubic crystals. *Engineering Fracture Mechanics*, *301*, p. 110023.

[18] Zhou, T., Zhu, L., Luo, X., Yu, J., Ye, C., Zhou, X., Tong, X., Chen, Z., Li, Y., Lin, J. and Wen, C., 2024. Effects of external staining on mechanical, optical, and biocompatibility properties of additively manufactured 3Y-TZP ceramic for dental applications. *Journal of Materials Research and Technology*, *31*, pp. 3961-3970.

[19] Moradkhani, A. and Baharvandi, H., 2018. Effects of additive amount, testing method, fabrication process and sintering temperature on the mechanical properties of Al2O3/3Y-TZP composites. *Engineering Fracture Mechanics*, *191*, pp. 446-460.

[20] Silling, S.A., Demmie, P.N. and Warren, T.L., 2007. *Peridynamic Simulation of High-Rate Material Failure* (No. SAND2007-3464C). Sandia National Lab.(SNL-NM), Albuquerque, NM (United States).

[21] Kilic, B. and Madenci, E., 2009. Peridynamic theory for thermomechanical analysis. *IEEE transactions on advanced packaging*, *33*(1), pp. 97-105.

[22] Platt, P., Mella, R., DeMaio, W., Preuss, M. and Wenman, M.R., 2017. Peridynamic simulations of the tetragonal to monoclinic phase transformation in zirconium dioxide. *Computational Materials Science*, *140*, pp. 322-333.

[23] Platt, P., Lunt, D., Polatidis, E., Wenman, M.R. and Preuss, M., 2016. In-situ digital image correlation for fracture analysis of oxides formed on zirconium alloys. *Corrosion Science*, *111*, pp. 344-351.

[24] Silling, S.A. and Lehoucq, R.B., 2010. Peridynamic theory of solid mechanics. *Advances in applied mechanics*, *44*, pp. 73-168.

[25] Budiansky, B., Hutchinson, J.W. and Lambropoulos, J.C., 1983. Continuum theory of dilatant transformation toughening in ceramics. *International Journal of Solids and Structures*, *19*(4), pp. 337-355.

[26] Yin, H., Gao, M. and Wei, R.P., 1995. Phase transformation and sustained load crack growth in ZrO2+ 3 mol% Y2O3: Experiments and kinetic modeling. *Acta metallurgica et materialia*, *43*(1), pp. 371-382.

[27] Xue, M., Liu, S., Wang, X. and Jiang, K., 2020. High fracture toughness of 3Y-TZP ceramic over a wide sintering range. *Materials Chemistry and Physics*, *244*, p. 122693.

[28] Jing, Q., Sun, J., Zhang, F., Lei, L. and Zhang, J., 2023. Residual stress distributions around indentations and crack in 3Y-TZP ceramics measured using piezo spectroscopy. *Ceramics International*, *49*(17), pp. 28256-28266.

[29] Vriami, D., Beaugnon, E., Erauw, J.P., Vleugels, J. and Van der Biest, O., 2015. Texturing of 3Y-TZP zirconia by slip casting in a high magnetic field of 17.4 T. *Journal of the European Ceramic Society*, *35*(14), pp. 3959-3967.

[30] Platt, A., Frankel, P., Gass, M., Howells, R. and Preuss, M., 2014. Finite element analysis of the tetragonal to monoclinic phase transformation during oxidation of zirconium alloys. *Journal of Nuclear Materials*, *454*(1-3), pp. 290-297.

[31] Fukuhara, M. and Yamauchi, I., 1993. Temperature dependence of the elastic moduli, dilational and shear internal frictions and acoustic wave velocity for alumina,(Y) TZP and β′-sialon ceramics. *Journal of materials science*, *28*(17), pp. 4681-4688.

[32] Moradkhani, A., Baharvandi, H. and Naserifar, A., 2019. Fracture toughness of 3Y-TZP dental ceramics by using vickers indentation fracture and SELNB methods. *Journal of the Korean Ceramic Society*, *56*(1), pp. 37-48.

[33] Wolten, G.M., 1963. Diffusionless phase transformations in zirconia and hafnia. *Journal of the American Ceramic Society*, *46*(9), pp. 418-422.

[34] Subbarao, E.C., Maiti, H.S. and Srivastava, K.K., 1974. Martensitic transformation in zirconia. *Physica status solidi (a)*, *21*(1), pp. 9-40.

[35] Eshelby, J.D., 1957. The determination of the elastic field of an ellipsoidal inclusion, and related problems. *Proceedings of the royal society of London. Series A. Mathematical and physical sciences*, *241*(1226), pp. 376-396.

[36] Díaz, M., Smirnov, A., Gutiérrez-González, C.F., Estrada, D. and Bartolomé, J.F., 2020. Microstructure and mechanical properties of zirconia (3Y-TZP)/Zr composites prepared by wet processing and subsequent spark plasma sintering. *Ceramics*, *3*(1), pp. 53-64.

[37] Vladislavova, L., Smolorz, T., Orlovskaya, N., Lugovy, M., Reece, M.J., Köbel, S., Kopia, A., Makowska, M., Graule, T. and Blugan, G., 2021. Strength analysis and stress-strain deformation behavior of 3 mol% Y-TZP and 21 wt.% Al_2O_3-3 mol% Y-TZP. *Materials*, *14*(14), p. 3903.

[38] Scardi, P., Leoni, M., Loch, M. and Barbezat, G., 2004, January. Elastic behaviour of thin stabilized-zirconia coatings. In *Materials Science Forum* (Vol. 443, pp. 77-82). Trans Tech Publications Ltd.

[39] Ni, N., Hudson, D., Wei, J., Wang, P., Lozano-Perez, S., Smith, G.D.W., Sykes, J.M., Yardley, S.S., Moore, K.L., Lyon, S. and Cottis, R., 2012. How the crystallography and nanoscale chemistry of the metal/oxide interface develops during the aqueous oxidation of zirconium cladding alloys. *Acta Materialia*, *60*(20), pp. 7132-7149.